PAPER

Improved adaptive genetic algorithm with sparsity constraint applied to thermal neutron CT reconstruction of two-phase flow

To cite this article: Mingfei Yan *et al* 2018 *Meas. Sci. Technol.* **29** 055404

View the article online for updates and enhancements.

Related content

IOP ebooks™

Bringing you innovative digital publishing with leading voices to create your essential collection of books in STEM research.

Start exploring the collection - download the first chapter of every title for free.

Improved adaptive genetic algorithm with sparsity constraint applied to thermal neutron CT reconstruction of two-phase flow

Mingfei Yan[1]**, Huasi Hu**[1,3] ⓘ**, Yoshie Otake**[1,2]**, Atsushi Taketani**[2]**,**
Yasuo Wakabayashi[2]**, Shinzo Yanagimachi**[2]**, Sheng Wang**[1,2]**, Ziheng Pan**[1]
and Guang Hu[1]

[1] School of Energy and Power Engineering, Xi'an Jiaotong University, Xi'an 710049,
People's Republic of China
[2] RIKEN, Wako, Saitama, 351-0198, Japan

E-mail: huasi_hu@mail.xjtu.edu.cn

CrossMark

Abstract

Thermal neutron computer tomography (CT) is a useful tool for visualizing two-phase flow due to its high imaging contrast and strong penetrability of neutrons for tube walls constructed with metallic material. A novel approach for two-phase flow CT reconstruction based on an improved adaptive genetic algorithm with sparsity constraint (IAGA-SC) is proposed in this paper. In the algorithm, the neighborhood mutation operator is used to ensure the continuity of the reconstructed object. The adaptive crossover probability P_c and mutation probability P_m are improved to help the adaptive genetic algorithm (AGA) achieve the global optimum. The reconstructed results for projection data, obtained from Monte Carlo simulation, indicate that the comprehensive performance of the IAGA-SC algorithm exceeds the adaptive steepest descent-projection onto convex sets (ASD-POCS) algorithm in restoring typical and complex flow regimes. It especially shows great advantages in restoring the simply connected flow regimes and the shape of object. In addition, the CT experiment for two-phase flow phantoms was conducted on the accelerator-driven neutron source to verify the performance of the developed IAGA-SC algorithm.

Keywords: two-phase flow, CT reconstruction, genetic algorithm, compressed sensing

(Some figures may appear in colour only in the online journal)

1. Introduction

Two-phase flow measurement is a significant and difficult task in nuclear energy and petroleum industries. The main parameters of two-phase flow include: flow regime, void fraction and density, etc. However, due to the variety of measured parameters as well as change over time, real-time imaging technology is needed. As one of the most popular methods, x-ray imaging has been widely applied in visualizing two-phase flow. Compared with x-ray radiography, computer tomography (CT) has the advantage of obtaining 3D information about the two-phase flow, therefore, it has attracted many researchers' and professionals' attention [1–3]. As the neutron has a bigger contrast of reaction cross section between water and air than that of x-rays, as well as having a strong penetrability for tube walls made of metallic material, a better contrast to noise ratio (CNR) can be obtained for the reconstructed image [4, 5].

CT reconstruction algorithms can be divided into two categories: analytical methods and iterative methods. The filter back projection (FBP) algorithm, as a kind of analytical

[3] Author to whom correspondence should be addressed.

1

method, is the most popular algorithm in the medical CT area. It requires much projection data, otherwise a number of streak artifacts will appear on the reconstructed image [6]. In contrast, iterative methods are especially suitable for incomplete view reconstruction with insufficient projection data. Incomplete view reconstruction can be subdivided into limited view reconstruction and few view reconstruction in actual application [7]. As the two-phase flow is dynamic and the tube cannot be rotated, the typical imaging configuration is based on combining a limited number of radiation sources and detector arrays around the tube. Therefore, only limited projection data can be collected, and the reconstruction is a typical few view reconstruction problem. The equation describing incomplete view CT reconstruction is ill-posed. The effective way to solve an ill-posed equation is to employ the iteration method with some kind of constraint conditions. Based on this principle, different algorithms, such as the simultaneous algebraic reconstruction technique (SART) [8], Landweber (LW) [9], conjugate gradient (CG) [10], maximum likelihood expectation maximization (MLEM) [11], maximum *a posteriori* (MAP) and multiplicative algebraic reconstruction technique (MART) [12] have been developed. The compressed sensing (CS) theory was formally put forward by Candes *et al* in 2004; according to this theory, the image is sparse in various domains [13, 14]. For CT reconstruction, the sparse prior make it possible to restore the image from scant projection data. By means of the sparsity in the gradient magnitude domain, Sidky *et al* published a powerfully adaptive steepest descent-projection onto convex sets (ASD-POCS) algorithm for CT reconstruction in 2006 and 2008 [6, 15]. In the two-phase flow CT reconstruction area, most researchers directly implemented reconstruction via the algorithms described above developed for medical CT [16, 17]. Although desirable results can be achieved, there is much space to enhance reconstruction accuracy. The genetic algorithm (GA), as a kind of the optimal algorithm, which was first put forward by Holland in 1975 [18], has provided a new perspective for incomplete view CT reconstruction. The evident advantages of the GA applied to CT reconstruction exhibit in two aspects: firstly, the continuity feature of the reconstructed object can be coupled into it conveniently; secondly, it searches solution space randomly, which has proved to be very effective in solving large and complex space cases [18, 19]. However, since the simple genetic algorithm (SGA) is easy to be trapped in the local optimum, the adaptive genetic algorithm (AGA) comes into being, in which crossover probability P_c and mutation probability P_m can be adjusted adaptively as fitness value changing to help the algorithm converge to the globally-optimal solution [20].

This paper combines the GA and CS theory to develop a novel algorithm for two-phase flow CT reconstruction. The contents are presented thus: firstly, a novel improved adaptive genetic algorithm with sparsity constraint (IAGA-SC) algorithm is proposed; secondly, the performance of the IAGA-SC algorithm is tested by reconstructing the projection data from Monte Carlo simulation; lastly, a CT experiment for two-phase flow phantoms is carried out on the accelerator-driven neutron source to verify the performance of the IAGA-SC algorithm.
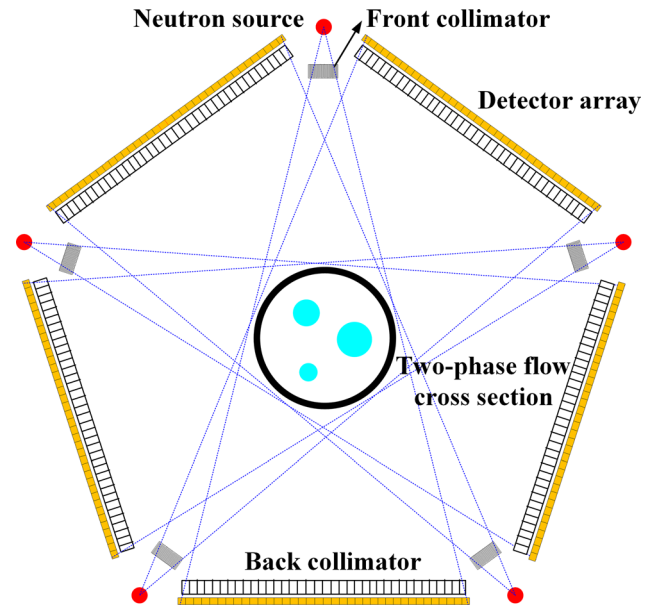

Figure 1. Thermal neutron CT of two-phase flow.

2. CT reconstruction principle and proposed IAGA-SC algorithm

2.1. Configuration of thermal neutron CT of two-phase flow

Inspired by the typical two-phase flow gamma ray CT setup mentioned in [21], as well as considering the development of the miniature neutron tube, a compact two-phase flow thermal neutron CT configuration is proposed, as outlined in figure 1. In the configuration, five neutron sources and detector arrays are combined for real-time imaging. Each detector array is made up of 37 pixels, and the pixel size is 4 mm × 4 mm × 0.05 mm (thickness) voxel. The reason for such a big pixel area is to reduce the exposure time, which is helpful for improving the real-time performance of two-phase flow CT. The material of the detector array is ^{6}LiF (ZnS: Ag), which has a relatively low sensitivity to gamma rays and fast neutrons. The semiconductor optical coupler is coupled on each detector pixel to transfer the light signal to the electric one. The purpose of the front collimator is to constrain the incident neutron beam to be fanned, and the back collimator is for reducing the scattered neutrons. The material of the two kind of collimators is B_4C (^{10}B:^{11}B = 1:4), which has a highly thermal neutron absorption cross section. In this paper, the simulation work is based on this configuration.

2.2. CT reconstruction principle

The principle of CT is the law of rays attenuated in the matter; when considering noise in the system, CT reconstruction can be regarded as:

$$P = WX + \delta \qquad (1)$$

where $P = [p_1, p_2, ..., p_M]$ is the projection vector; $W = (w_{ij}) \in W^M \times W^{N \times N}$ is the system matrix, which is determined by the geometry of the CT system; $X = [x_1, x_2, ..., x_{N \times N}]$ is the image vector to be solved, and δ refers to the noise. The

purpose of the CT reconstruction is to solve equation (1); in the few-view reconstruction problem, $M \ll N \times N$, the equation is underdetermined and the solution is easily disturbed by the noise.

2.3. System matrix computation

The previous step before implementing CT reconstruction is the computing system matrix *W*. There are three different models for the system matrix computation: point, line and area model. The computing system matrix with point model is time saving but easily introduces artifacts to the reconstructed image, while the area model is accurate but time consuming. In contrast, the line model is relatively accurate and time saving [22, 23], hence it is employed to compute the system matrix in this paper. For the line model, the weight coefficient w_{ij} in the system matrix is the intersection length between the *i*th ray and the image *j*th pixel. The ray-driven way is used to compute the system matrix with the line model, and an acknowledged procedure of this way is raised by Siddon [24]. In reconstruction, because the number of total projection data is only 185 (37 × 5), they are extended to 2255(451 × 5) by three times the Amy's interpolation method to obtain a reconstructed image with high quality [25]. In the interpolation process, the inserted points uniformly distribute from the *1st* pixel to the *37th* pixel in each direction. Then the corresponding number and location of 'virtual rays' are employed to compute the system matrix. The summation of the system matrix according to five directions is shown in figure 2, where the size of reconstructed area is 70.7 mm × 70.7 mm (199 pixel × 199 pixel).

2.4. Prior information of two-phase flow

Generally speaking, when implementing the CT reconstruction, the more prior information we can dig out, the more accuracy we can get for the reconstructed image. The reconstructed object in this current research is the two-phase flow, and the prior information is listed below:

- Binary value: two-phase flow is made up of two phases, and we can regard that the water is 1 and gas is 0 on the image respectively.
- Continuity and sparsity: spatial distribution of each phase in the two-phase flow is continuous physically; in other words, the two-phase flow is naturally sparse in some kind of domains mathematically.
- The boundary is known: the two-phase flow is located in the tube and the size of the tube is known, thus the area boundary of the reconstructed image is determined.

In the IAGA-SC algorithm, the upper prior information is utilized to improve the reconstructed image quality and speed up the convergence of the algorithm.

2.5. Proposed IAGA-SC algorithm

The GA simulates the process of organisms evolving in nature. The main concepts of the GA include population, individual,
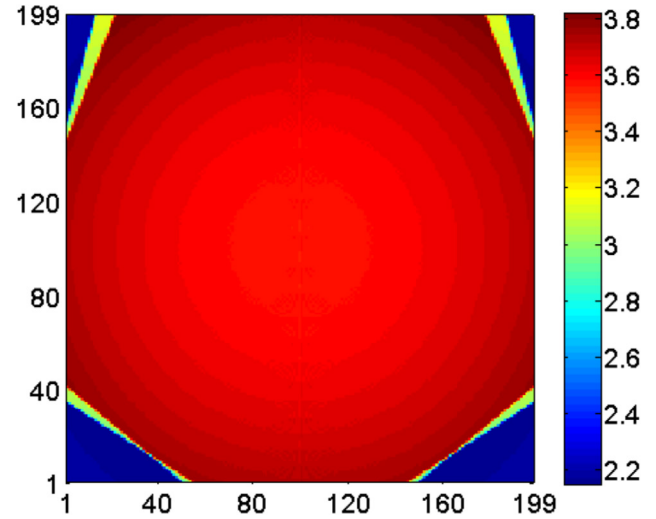

Figure 2. Summation of system matrix according to five directions.

parent, offspring, fitness function, selection, crossover, and mutation, etc [18]. In the case of the GA being applied to image reconstruction, each individual refers to one image to be reconstructed, and all individuals make up one population. According to Darwin's theory of evolution, the individual with a higher fitness value has a bigger probability of being selected in each generation. The selected individuals continue participating in crossover and mutation processes, then offspring is produced to form the next generation eventually. In essence, the evolution of the individual in the GA is under the control of selection, crossover and mutation operators. A detailed description of the fitness function and evolution strategy used in the developed IAGA-SC algorithm will be discussed in sections 2.5.1 and 2.5.2 respectively.

2.5.1. Fitness function of the IAGA-SC algorithm.

Since the fitness function is used to evaluate the survival ability of the individual, which determines the evolution direction of the individual, it is crucial to construct it for the two-phase flow CT reconstruction. In this paper, apart from the reconstructed image meeting the projection data consistency condition, the sparsity constraint is utilized. The reconstruction is regarded as a multi-objective optimization problem. In order to optimize the multi-objective, we convert it to the single one by linear weighted summation:

$$g = \|P - WX\|_2^2 + \alpha \|\Psi X\|_n \qquad (2)$$

where $\|\Delta\|_n$ is the l_n-norm of vector $\Delta(n = 0, 1, 2)$; $\|P - WX\|_2^2$ is the fidelity term and $\|\Psi X\|_n$ is the sparsity constraint term (or regularization term); $\alpha \in (0, 1)$.

For the two-phase flow, several expressions can describe its sparse feature: the total difference (TD) [26], weighted total difference (WTD) [27], L0-norm of the gradient magnitude of the image (GMI-L0) and L1-norm of the gradient magnitude of the image (GMI-L1). The L1-GMI is the so-called total variation (TV) [6]. The detailed expressions of each sparse mode are listed in table 1, where *s* and *t* are the pixel indexes. The TD is actually the anisotropic TV.

Table 1. Sparse representation of two-phase flow.

Sparse models	Expressions
TD	$\sum_{s,t}\left(\left\|x_{s,t}-x_{s-1,t}\right\|+\left\|x_{s,t}-x_{s,t-1}\right\|\right)$
WTD	$\sum_{s,t}\left(\left\|x_{s,t}-x_{s-1,t}\right\|+\left\|x_{s,t}-x_{s,t-1}\right\|+\beta\left(\left\|x_{s,t}-x_{s-1,t-1}\right\|+\left\|x_{s-1,t}-x_{s,t-1}\right\|\right)\right)$
GMI-L0	$\sum_{p}\#\left\{p\,\middle\|\,\left\|x_{s,t}-x_{s-1,t}\right\|+\left\|x_{s,t}-x_{s,t-1}\right\|\neq 0\right\}$
GMI-L1(TV)	$\sum_{s,t}\sqrt{\left(x_{s,t}-x_{s-1,t}\right)^{2}+\left(x_{s,t}-x_{s,t-1}\right)^{2}}$
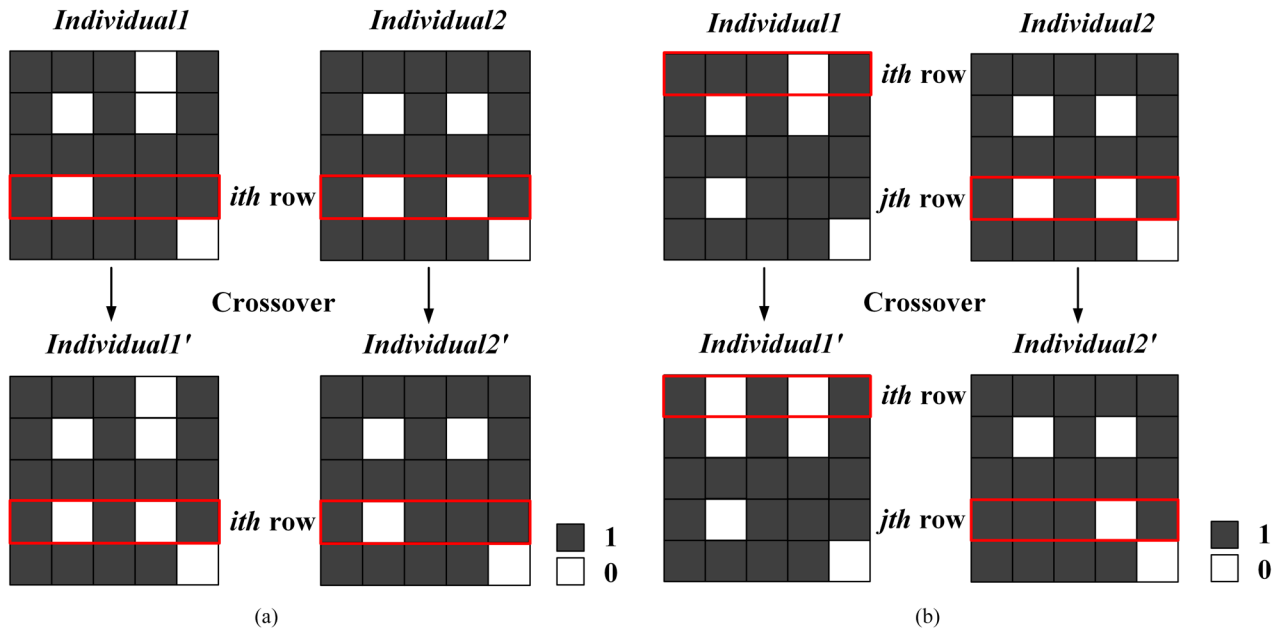
Figure 3. R/C crossover. (a) Uniform crossover. (b) Random crossover.

Although both the TD and TV share a similar sparsity feature, the TD shows an advantage in terms of incomplete view CT reconstruction [28]. The TV and TD seek the gradient sparsity horizontally and vertically. The WTD is an improvement of the TD; it does not only seek the gradient sparsity horizontally and vertically, but also diagonally, which can improve the performance of the algorithm to restore sharp edges of the image. β is the weight between diagonal directions and horizontal, vertical directions; it is 1.0 in this paper. The GMI-L0 is a more accurate expression of gradient sparsity than the GMI-L1 (TV), since it only counts the number of non-zero gradients and the gradient magnitude will not be counted, thus the large gradient magnitude will not be penalized. However, because the L0 problem is usually NP hard, it is always transferred to the L1 problem, that is why TV is more popular than the GMI-L0. By the IAGA-SC algorithm proposed in this paper, the strategy to solve L0 and L1 problems is similar. In other words, no matter what the sparse expressions are, they can be solved by our algorithm.

The fitness function is described as the inverse of the objective function by multiplying a certain number, thus the optimal object is to maximize the fitness function:

$$f = \frac{b}{g} \tag{3}$$

where b is the scaling parameter of the fitness function.

2.5.2. Evolution strategy of the IAGA-SC algorithm. The selection operator determines how the individuals are selected, which determines the efficiency and convergence of the algorithm. In this paper, a selection operator based on the stochastic tournament with simulated annealing idea is utilized, and the elitist model is employed to guarantee the survival of the best individual [29]. The selection mechanism and processes are as described below.

① Selecting T individuals from the current generation, and then comparing the fitness value of the selected individuals.
② Producing a random number between 0 and 1; if it is less than p_0, the individual with maximum fitness value obtained in procedure ① is selected, or else an individual is selected randomly.
③ Repeating ① and ② P times, P individuals for the parent generation are selected.
④ The individual with the minimal fitness value in the offspring generation is directly replaced by one with maximum fitness value in the parent generation.

The crossover operator is the main method of producing the offspring generation from the parent generation. The algorithm with a good crossover operator possesses powerful global searching ability. The crossover operator in the proposed algorithm is uniform and random R/C crossover [30]. As is shown in figure 3(a), the uniform R/C crossover processes are as detailed below.
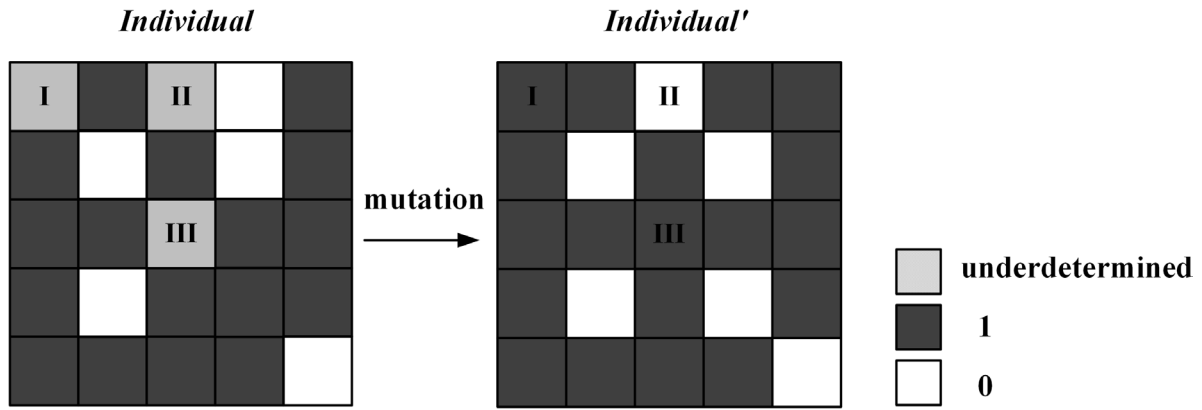
Figure 4. Neighborhood mutation.

① Producing a random integer between 0 and 1; if it is equal to 0, the crossover operator acts on the row of the individual, or else acts on the column.

② Producing another random number between 0 and 1, if it is less than the crossover probability P_c, the mutation operator is activated for the selected individuals participating in the crossover.

③ Producing another random integer between 0 to N (N is the number of rows or columns of the image to be reconstructed), which is regarded as the location of the crossover.

④ Exchanging the row or column with the same location for the selected individuals to produce the offspring.

The difference between random and uniform R/C crossover lies in the procedure ③ described above. In random crossover, two random integers are produced for a pair of selected individuals, which jointly determine the location of the crossover (see figure 3(b)).

The mutation operator is the auxiliary method of producing the offspring generation, which determines the local searching ability of the algorithm. Another function of the mutation operator is to restrain premature phenomena from occurring. The mutation operator in the proposed algorithm is neighborhood mutation [30], which ensures the continuity of the reconstructed object. The mechanism of neighborhood mutation is shown in figure 4 (for 5×5 pixels as an example). According to the number of neighborhood pixels, the pixels can be divided into three kinds: corner pixels (I), boundary pixels (II) and other pixels (III). Each corner pixel has three neighborhood pixels, each boundary pixel has five neighborhood pixels, and each other pixel has eight neighborhood pixels. The mutation processes are detailed below.

① Producing a random number between 0 and 1, if it is less than the mutation probability P_m, the mutation operator is activated for the pixel.

② Calculating the mean value A of this pixel's neighborhood pixels, then producing another random number between 0 and 1, if the random number is less than A, the value of this pixel changes to 1, otherwise, it changes to 0.

Due to the fact that the searching space is large (199×199) in our CT reconstruction, the AGA is easy to be trapped in

the local optimum. To avoid such a disadvantage, the cross probability P_c and mutation probability P_m for the IAGA-SC algorithm have been improved based on [20]:

$$P_c = \begin{cases} \dfrac{P_{c1}\left(f_{avg}-f'\right)+P_{c2}\left(f'-f_{min}\right)}{f_{avg}-f_{min}} & f' < f_{avg} \\[3mm] \dfrac{P_{c2}\left(f_{max}-f'\right)+P_{c3}\left(f'-f_{avg}\right)}{f_{max}-f_{avg}} & f' \geqslant f_{avg} \end{cases} \tag{4}$$

$$P_m = \begin{cases} \dfrac{P_{m1}\left(f_{avg}-f\right)+P_{m2}\left(f-f_{min}\right)}{f_{avg}-f_{min}} & f < f_{avg} \\[3mm] \dfrac{P_{m2}\left(f_{max}-f\right)+P_{m3}\left(f-f_{avg}\right)}{f_{max}-f_{avg}} & f \geqslant f_{avg} \end{cases} \tag{5}$$

where f' is the bigger fitness value of selected individuals participating in the crossover, and f is the fitness value of the selected individual participating in the mutation. f_{min}, f_{avg} and f_{max} denote the minimum, average and maximum fitness values of the population respectively. $P_{c1} > P_{c2} > P_{c3} \in (0,1)$, $P_{m1} > P_{m2} > P_{m3} \in (0,1)$.

Figure 5 shows the comparison of the adaptive P_c and P_m between our proposed algorithm and [20]. In both formulas, P_c and P_m will follow the linear adjustment as individual fitness value f and f' vary from f_{avg} to f_{max}. However, they will keep a constant number as f and f' vary from f_{min} to f_{avg} in [20], thus easily trapping the algorithm in the local optimum. In contrast, in the improved one, they will also follow the linear adjustment in this case. If f' and f are close to f_{min}, P_c and P_m will increase to be bigger values; in contrast, if f' and f are close to f_{avg}, P_c and P_m will decrease to be relatively smaller values. Hence the algorithm can escape from local optimum with bigger probability. Moreover, when f and f' are equal to f_{max}, P_c and P_m are zero according to [20], which means that the optimal individual in the current generation will no longer participate in crossover and mutation processes, thus the premature phenomenon easily occurs. In contrast, P_c and P_m will keep a non-zero constant in the improved one, which means the optimal individual still has a certain probability of participating in the evolution.

2.5.3. Main procedures of the IAGA-SC algorithm. The main procedures of the two-phase flow CT reconstruction by the IAGA-SC algorithm are as follows.
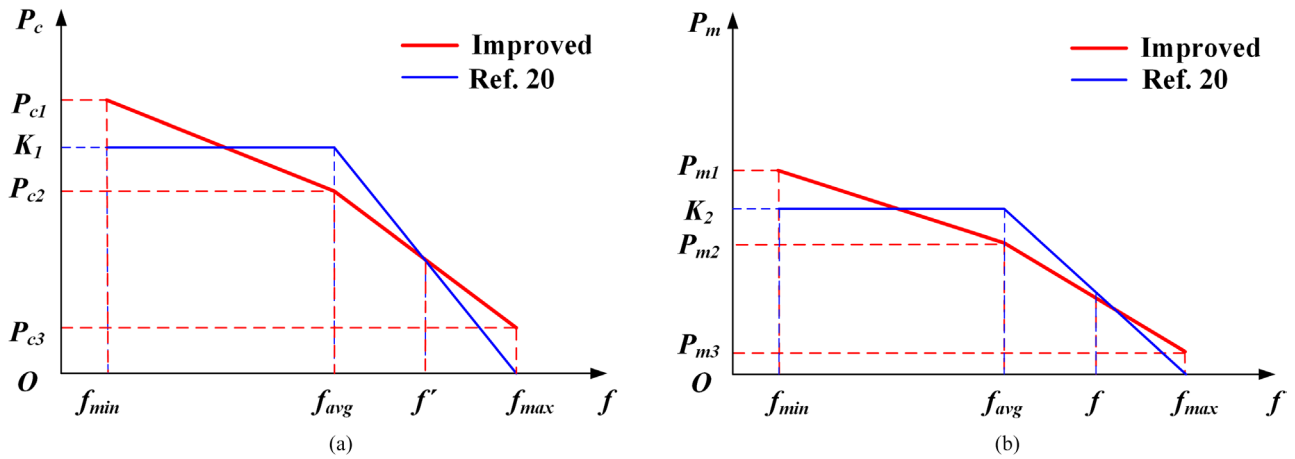
Figure 5. Improvement of adaptive P_c and P_m.

Table 2. Parameters of the IAGA-SC algorithm.

Parameters	Values
Population size (P)	50
Maximum generation (G)	10 000
Size of stochastic tournament (T)	3
Maximum stagnancy generation (S)	1000
α	7×10^{-9}
b	1.0
p_0	0.75
P_{c1}	0.9
P_{c2}	0.5
P_{c3}	0.1
P_{m1}	0.1
P_{m2}	0.05
P_{m3}	0.005

(1) Initialing the pixel value of the image to be reconstructed randomly by zero or one.
(2) Computing the fitness value f by projection vector P, system matrix W and initialed image (1st iteration) or evolved image (from 2nd iteration).
(3) Evolving by selection, crossover and mutation operators.
(4) Preserving the best individual if it was produced in the evolution.
(5) Looping (2)–(4) until meeting the convergence condition (either the maximum generation (G) or maximum stagnancy generation (S) in this paper).

The pseudo code of the above procedures is shown in the appendix of this paper. The parameters utilized in the IAGA-SC algorithm are listed in table 2.

2.5.4. Evaluation index of reconstructed image quality. In order to evaluate the reconstructed image quality quantitatively, and further evaluate the performance of the reconstruction algorithm, two indexes, the correlation coefficient c and normalized mean square distance d, are introduced [31]:

$$c = \frac{\sum_{i=1}^{N} (r_i - \bar{r}_i)(o_i - \bar{o}_i)}{\sqrt{\sum_{i=1}^{N} (r_i - \bar{r}_i) \sum_{i=1}^{N} (o_i - \bar{o}_i)}} \quad (6)$$

$$d = \sqrt{\frac{\sum_{i=1}^{N} (r_i - o_i)^2}{\sum_{i=1}^{N} (r_i - \bar{o}_i)^2}} \quad (7)$$

where r_i and o_i are the pixel values of the reconstructed and original image respectively, and $\bar{r}_i$ and $\bar{o}_i$ are the average ones.
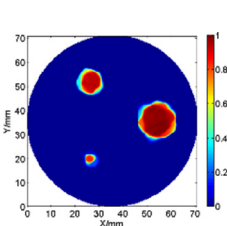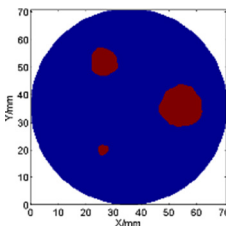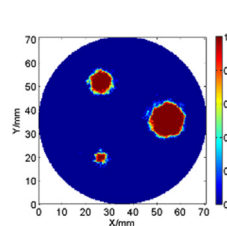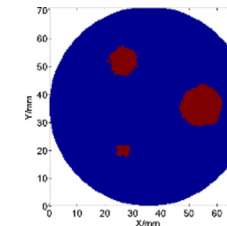
3. Performance of the IAGA-SC algorithm
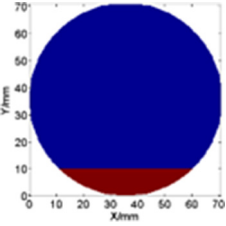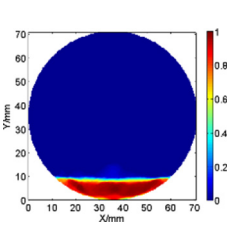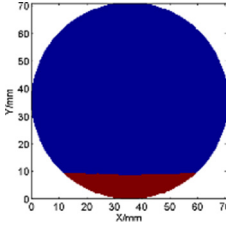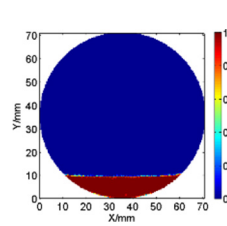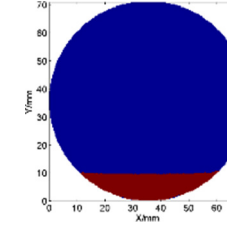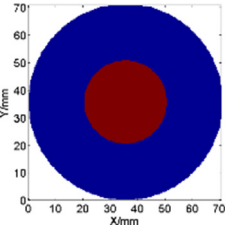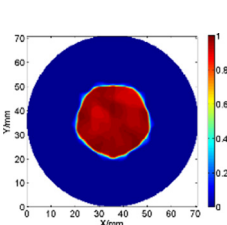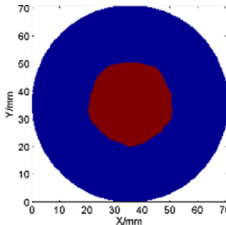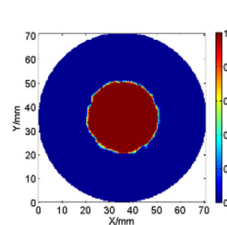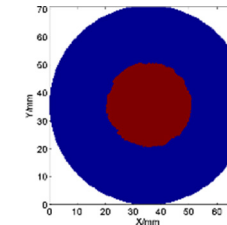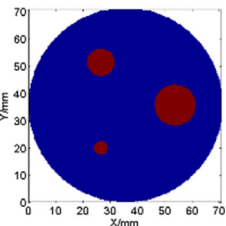
3.1. Projection data simulation

The MCNP code, developed by the Los Alamos National Laboratory, is employed to implement simulation of the process of neutrons transportation in matter. In the simulation, the energy of incident neutrons is 0.0253 eV, which is sampled with a 13.4 degree bias angle. The total number of incident neutrons is 120 million (24 million for each source) with the biggest statistical deviation of detector pixel below 5%. F4 and Fm cards are combined to record the energy deposition of secondary alpha and tritium particles in the detector. The inner diameter of the two-phase flow tube simulated is 70.7 mm. The tube wall material is carbon steel with a thickness of 2.8 mm.

3.2. Reconstruction for typical and complex flow regimes

In order to demonstrate the performance of the IAGA-SC algorithm in the image reconstruction of two-phase flow CT, typical flow regimes, stratified, core and 'bubble' flow, are employed as the reconstruction objects. The 'bubble' in this paper denotes that the shape of the object is similar to a bubble. As the GA is a kind of random searching algorithm, many random numbers are used in it; the optimal results may be different for repeated computations. For the IAGA-SC algorithm, to avoid such a disadvantage, the average image of five times reconstruction is regarded as the ultimately reconstructed image. In consideration of the binary feature of the two-phase flow, the average image through binarization is also shown as the comparison. The binarization method is the famous Otsu algorithm [32]. Table 3 shows reconstructed images of typical flow regimes. The red and blue parts on the reference image represent water and air respectively. Because the TV is the most popular sparsity mode, if there is no

Table 3. Reconstructed results of typical flow regimes.

Reference	ASD-POCS	Binarization	IAGA-SC	Binarization
Stratified	$c = 0.9396, d = 0.3683$	$c = 0.9197, d = 0.3947$	$c = 0.9802, d = 0.1986$	$c = 0.9747, d = 0.2241$
Core	$c = 0.982, d = 0.1935$	$c = 0.9754, d = 0.2217$	$c = 0.9864, d = 0.1641$	$c = 0.9816, d = 0.1921$
Three 'bubbles'	$c = 0.9364, d = 0.358$	$c = 0.908, d = 0.427$	$c = 0.9354, d = 0.3537$	$c = 0.912, d = 0.4167$

specific explanation, the TV is the sparsity constraint term in equation (2) in this paper. To show the excellent performance of the IAGA-SC algorithm, the robust ASD-POCS algorithm is selected as the comparison, which can guarantee a fair comparison due to both the two algorithms employing the same TV sparsity constraint model. It is important to ensure the comparison between the IAGA-SC and ASD-POCS algorithms is fair. A rigorous way to carry out such a comparison is to compare the images reconstructed by each algorithm with the optimal parameters. Although the reference image can be regarded as a known condition in comparing algorithms, the selection of optimal parameters is always complex and time consuming due to the fact that the number of parameters in the algorithm is usually more than one; moreover, the optimal parameters are usually different for different reconstructed objects. As the ASD-POCS algorithm has eight parameters (see table 5), one realistic and feasible parameter selection method is to transfer the multi-dimensional search problem into a one-dimensional one [33]. Specifically speaking, we vary ε while keeping the other seven parameters unchanged. The initial values of them are: $ng = 20$, $\alpha = 0.2$, $\alpha_{red} = 0.95$, $\beta = 0.005$, $\beta_{red} = 0.995$, $r_{max} = 0.95$, iter $= 120$. Thus the optimal ε can be discovered in a one-dimensional case, in which the lowest d is regarded as the selection standard. Then seven parameters are left to be optimized, and their optimal values can be figured out by the same way. It is worth mentioning that the set of parameters selected by such a way may not be the really optimal ones, and we term them as 'relatively

optimal parameters'. Table 5 shows the selected parameters for different reconstructed objects appearing in this paper. Additionally, the reference image is always unknown in the actual case, so the parameters for the IAGA-SC algorithm just employ the uniform numbers (shown in table 2). Although such action may not be very fair for the IAGA-SC algorithm, it is reasonable if the performance of the IAGA-SC algorithm can exceed the ASD-POCS algorithm in this case.

From table 3, it can be observed that the image reconstructed by the ASD-POCS algorithm is complete grayscale and 'stage block' artifacts appear on the image (see core flow in table 3). The reason for this is that the ASD-POCS algorithm employs the ART (or SART) algorithm to obtain the preliminary image and then makes use of the steepest descent method to decrease the TV of the image, which results in the piecewise smooth feature of the reconstructed image. In addition, the image reconstructed by the IAGA-SC algorithm is a generally binary value with partially non-binary information in the border regions. That is because the reconstruction process is under the binary model and the non-binary information is just introduced by the five times average. For the three kinds of flow regimes, the IAGA-SC algorithm exhibits a higher reconstruction accuracy than the ASD-POCS algorithm, especially for stratified flow. This is because it is simply connected and the IAGA-SC algorithm is easy to search out the optimal result. Compared with the ASD-POCS algorithm with binarization, the IAGA-SC algorithm with binarization can show much better results owing to the generally binary feature of the

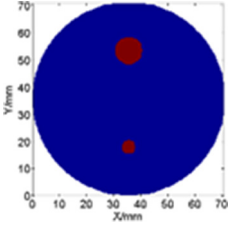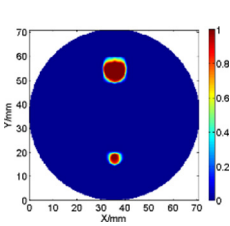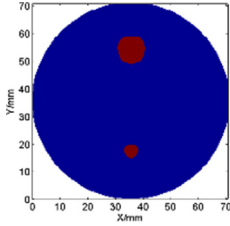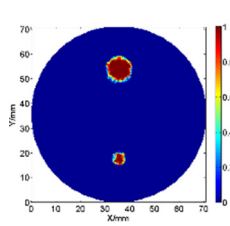**Table 4.** Reconstructed results of complex flow regimes.
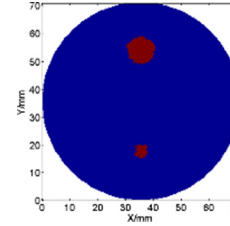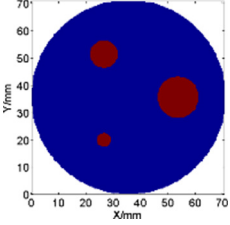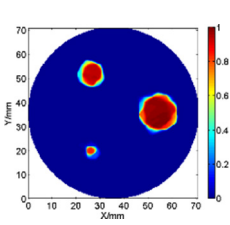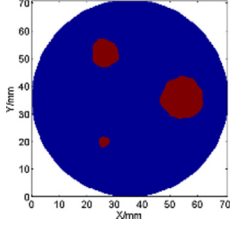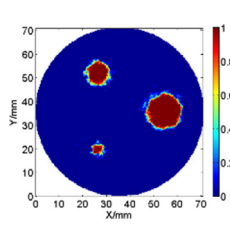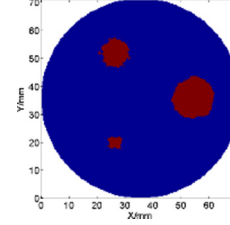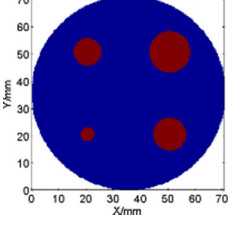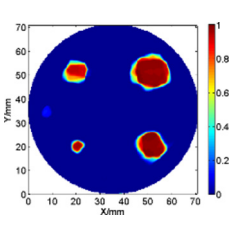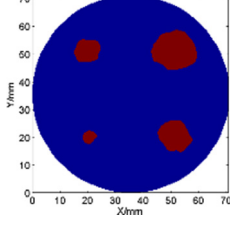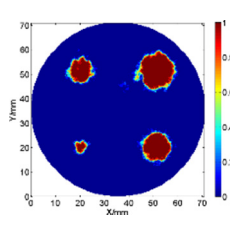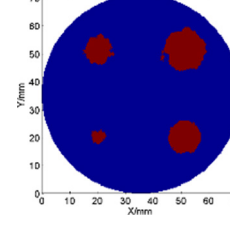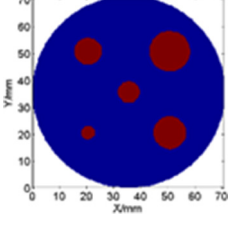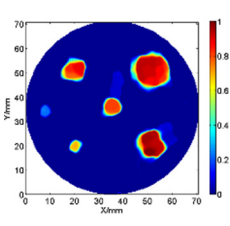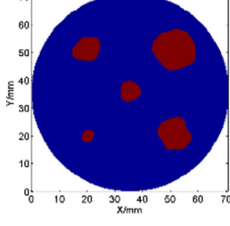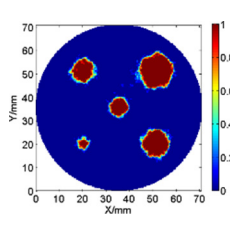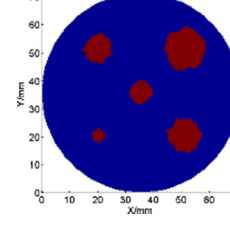
Reference	ASD-POCS	Binarization	IAGA-SC	Binarization
Two 'bubbles'	$c = 0.9271, d = 0.3754$	$c = 0.8902, d = 0.4721$	$c = 0.93, d = 0.3696$	$c = 0.8958, d = 0.4508$
Three 'bubbles'	$c = 0.9364, d = 0.358$	$c = 0.908, d = 0.427$	$c = 0.9354, d = 0.3537$	$c = 0.912, d = 0.4167$
Four 'bubbles'	$c = 0.9164, d = 0.4066$	$c = 0.8906, d = 0.4616$	$c = 0.9235, d = 0.3838$	$c = 0.9004, d = 0.4436$
Five 'bubbles'	$c = 0.9106, d = 0.4345$	$c = 0.8852, d = 0.4723$	$c = 0.9308, d = 0.3657$	$c = 0.9052, d = 0.4325$

image reconstructed by the IAGA-SC algorithm. Moreover, the ability of the IAGA-SC algorithm to restore the shape of the 'bubble' is much better (see core flow in table 3), and it will be further proved in complex flow regimes reconstruction.

Table 4 shows the reconstructed images of complex flow regimes, in which the number of 'bubbles' ranges from two to five, and the smallest and biggest size of the 'bubbles' is 5 mm and 15 mm respectively. From the reconstructed images, it can be observed that the IAGA-SC algorithm also shows better performance than the ASD-POCS algorithm in complex flow regimes reconstruction, especially the results through the binarization process. Moreover, the advantage of the IAGA-SC algorithm is inclined to be more obvious as the number of 'bubbles' increases. In addition, the IAGA-SC algorithm has also shown better ability to restore the shape of the 'bubble' than the ASD-POCS algorithm.
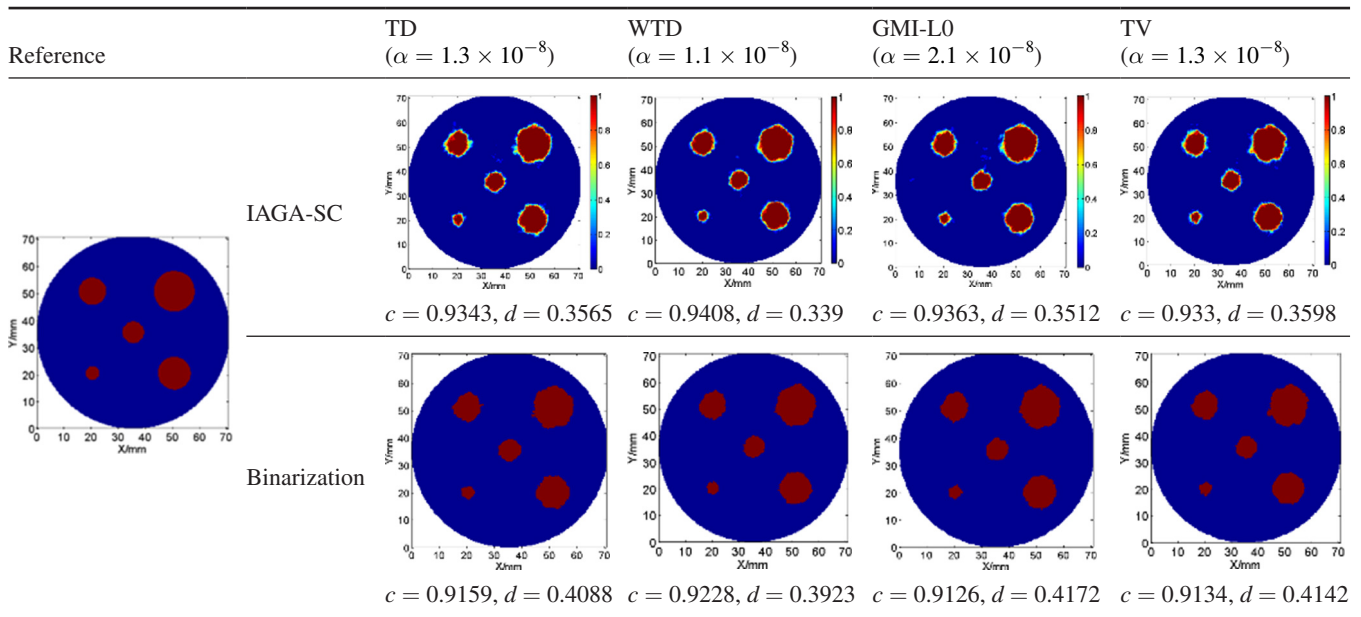
3.3. Comparison of reconstructed images with different sparsity constraints

Table 6 shows the comparison of reconstructed images of five 'bubbles' flow with different sparsity constraints: TD, WTD, GMI-L0 and TV. To ensure a fair comparison, we select the optimal sparsity constraint parameter α for each sparsity constraint model and keep other parameters the same, in which the selection standard is also lowest d. As expected, the performance of the WTD is better than the TD, the GMI_L0 is better than the TV and the TD is better than the TV, the reasons for which have been explained in section 2.5.1. The results in this paper also demonstrate that the performance of the WTD is better than the GMI_L0, which means the effect of improving the reconstruction accuracy by adding seeking the gradient sparsity diagonally is greater than penalizing the number of non-zero gradients.

Table 5. Selected relatively optimal parameters for the ASD-POCS algorithm.

Flow regimes	Relatively optimal parameters
Stratified	$\varepsilon = 0.001$, $ng = 10$, $\alpha = 0.2$, $\alpha_{\text{red}} = 0.95$, $\beta = 0.005$, $\beta_{\text{red}} = 0.995$, $r_{\max} = 0.95$, iter $= 120$
Core	$\varepsilon = 0.001$, $ng = 40$, $\alpha = 0.2$, $\alpha_{\text{red}} = 0.95$, $\beta = 0.1$, $\beta_{\text{red}} = 0.995$, $r_{\max} = 0.95$, iter $= 120$
Two 'bubbles'	$\varepsilon = 0.001$, $ng = 140$, $\alpha = 0.02$, $\alpha_{\text{red}} = 0.95$, $\beta = 0.005$, $\beta_{\text{red}} = 0.99$, $r_{\max} = 0.8$, iter $= 150$
Three 'bubbles'	$\varepsilon = 0.001$, $ng = 90$, $\alpha = 0.3$, $\alpha_{\text{red}} = 0.95$, $\beta = 0.007$, $\beta_{\text{red}} = 0.995$, $r_{\max} = 0.95$, iter $= 160$
Four 'bubbles'	$\varepsilon = 0.001$, $ng = 80$, $\alpha = 0.2$, $\alpha_{\text{red}} = 0.95$, $\beta = 0.005$, $\beta_{\text{red}} = 0.995$, $r_{\max} = 0.95$, iter $= 120$
Five 'bubbles'	$\varepsilon = 0.001$, $ng = 70$, $\alpha = 0.2$, $\alpha_{\text{red}} = 0.95$, $\beta = 0.005$, $\beta_{\text{red}} = 0.995$, $r_{\max} = 0.95$, iter $= 120$
Core (experiment)	$\varepsilon = 0.001$, $ng = 90$, $\alpha = 10$, $\alpha_{\text{red}} = 0.95$, $\beta = 0.003$, $\beta_{\text{red}} = 0.99$, $r_{\max} = 0.9$, iter $= 130$
Three 'bubbles' (experiment)	$\varepsilon = 0.001$, $ng = 100$, $\alpha = 15$, $\alpha_{\text{red}} = 0.95$, $\beta = 0.004$, $\beta_{\text{red}} = 0.995$, $r_{\max} = 0.95$, iter $= 120$

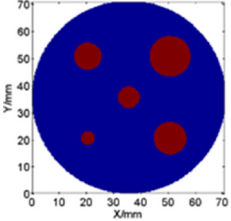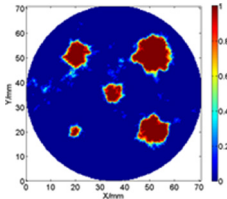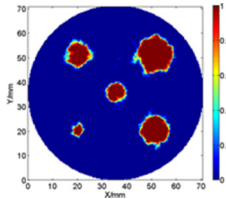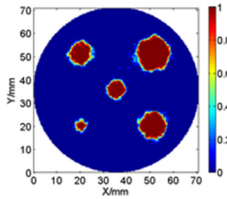**Table 6.** Reconstructed results with different sparsity constraints.

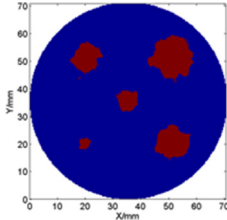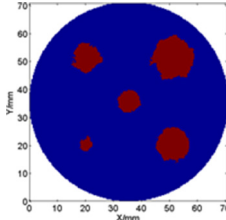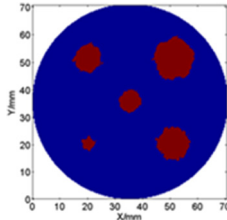| Reference		TD $(\alpha = 1.3 \times 10^{-8})$	WTD $(\alpha = 1.1 \times 10^{-8})$	GMI-L0 $(\alpha = 2.1 \times 10^{-8})$	TV $(\alpha = 1.3 \times 10^{-8})$
	IAGA-SC	$c = 0.9343$, $d = 0.3565$	$c = 0.9408$, $d = 0.339$	$c = 0.9363$, $d = 0.3512$	$c = 0.933$, $d = 0.3598$
	Binarization	$c = 0.9159$, $d = 0.4088$	$c = 0.9228$, $d = 0.3923$	$c = 0.9126$, $d = 0.4172$	$c = 0.9134$, $d = 0.4142$

3.4. Effect of statistical noise on images reconstructed by the IAGA-SC algorithm

Statistical noise is the main noise when employing practical projection data to implement CT reconstruction. It is subject to Poisson distribution, and it is big when the number of neutrons received by the detector pixels is insufficient. Table 7 shows a comparison of reconstructed images under different incident intensities; here the incident intensity refers to the number of neutrons emitted from each source, as shown in figure 1. The biggest deviation of detector pixels for 0.24 million, 2.4 million and 24 million are about 50%, 16% and 5% respectively. From table 7, it can be seen that the reconstructed image quality increases as the noise level decreases. However, when the biggest deviation of detector pixels varies

from 5% to 50%, the correlation coefficient of non-binary results just decreases from 0.9308 to 0.9016. The variation is not as evident as we expected. In other words, the IAGA-SC has a good property in resisting statistical noise. In addition, it can be observed that the results through the binarization process may become much worse, although the non-binary results are better (see the 2.4 million and 24 million case in table 7), in contrast to the comparison between the ASD-POCS and IAGA-SC algorithms shown in tables 3 and 4. The reason for this is that the binarization process is complex and the binary results depend on the details of the corresponding non-binary images. Therefore, in this paper, making a comparison between the ASD-POCS and IAGA-SC algorithms is based on non-binary and binary results, while making a

Table 7. Reconstructed results of the 'bubble' flow under different incident intensities.

Reference		0.24 million (50%)	2.4 million (16%)	24 million (5%)
	IAGA-SC	$c = 0.9016$, $d = 0.433$	$c = 0.9262$, $d = 0.3773$	$c = 0.9308$, $d = 0.3657$
	Binarization	$c = 0.8783$, $d = 0.49$	$c = 0.9061$, $d = 0.4306$	$c = 0.9052$, $d = 0.4325$

Figure 6. Configuration of the RANS.

comparison for other cases (like different sparsity constraints and statistical noise level) with the same IAGA-SC algorithm is only based on the non-binary results; the binary results are just shown as references in this case.

4. Experimental verification

The CT experiment for the two-phase flow was conducted on the RIKEN accelerator-driven neutron source (RANS). The configuration of the RANS is shown in figure 6, in which neutrons are produced by the Be (p, n) reaction with 7MeV protons bombarding the beryllium target. The advantages of the RANS are its compactness and flexibility. Its eventual goal is to be equipped onto trucks and employ neutrons to inspect

the safety condition of bridges and buildings by radiography and tomography.

Figure 7 shows the energy spectrum at 5 m away from the moderator (camera box location, which is on the left side of the neutron beam line). There are two peaks—the thermal neutron (25 meV) and the fast neutron (1MeV) peaks on the spectrum—and both of the intensities are near 10^4 cm$^{-2} \cdot$ s^{-1}. Therefore, it can be used for thermal and fast neutron imaging with different kinds of neuron detectors.

In the present experiment, two-phase flow phantoms have been manufactured to represent real two-phase flow, in which polymethyl methacrylate (PMMA) material with 1.18 g·cm^{-3} density is the substitute for real water. Core and 'bubble' flow phantoms are used as imaging objects in this experiment. The
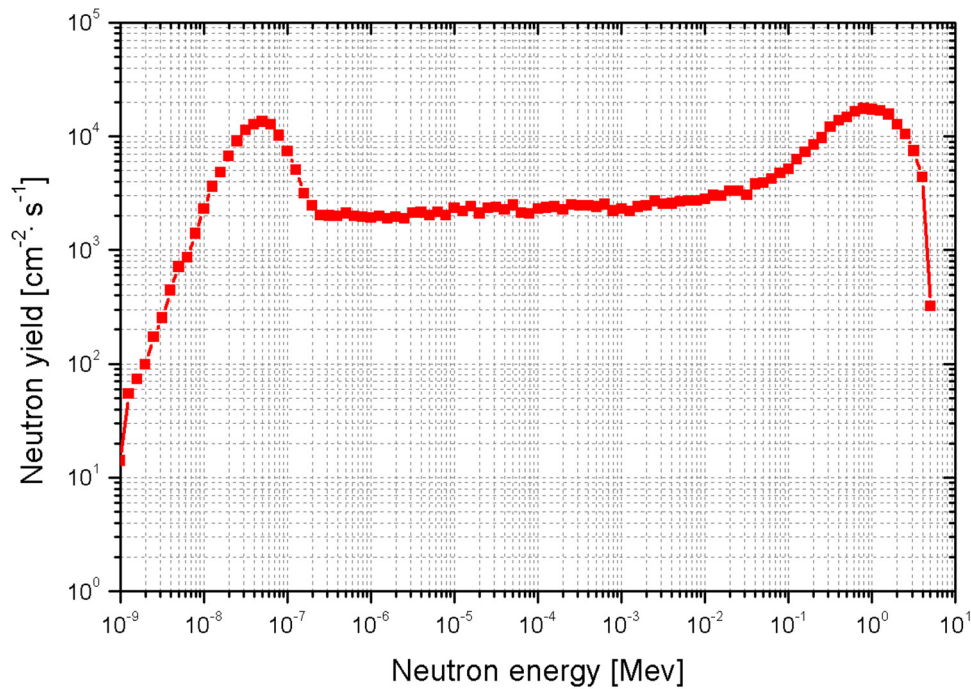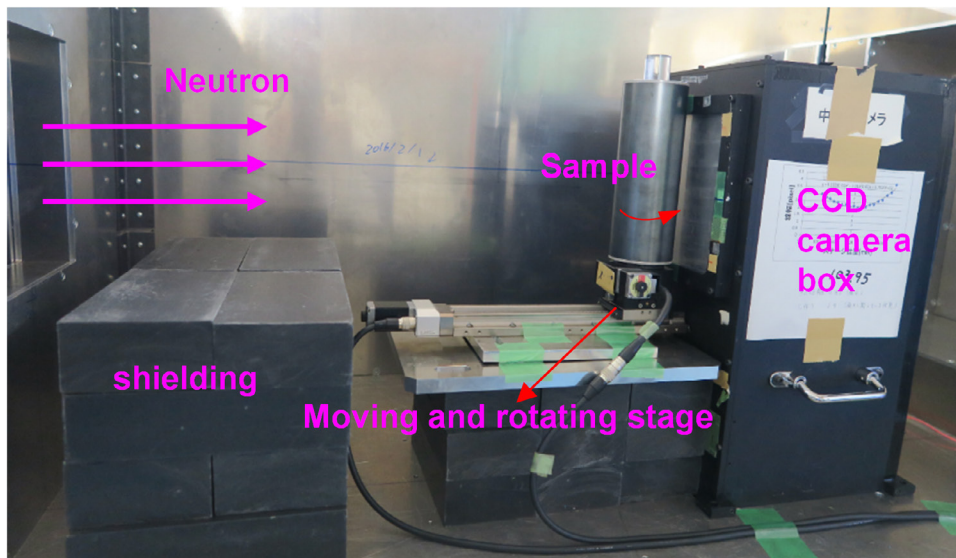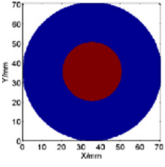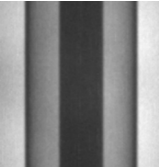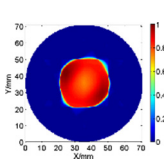
Figure 7. Neutron energy spectrum of the RANS.
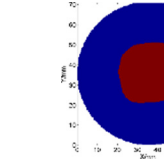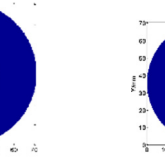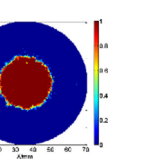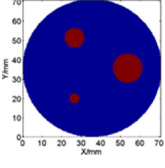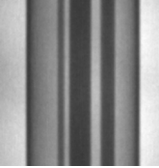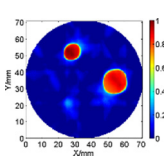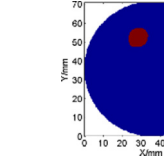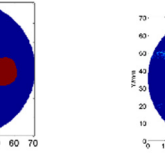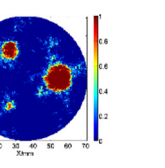
Figure 8. Neutron radiography setup.

neutron radiography setup is shown in figure 8, and all the components are equipped in the camera box of the RANS. The size of the ^{6}LiF (ZnS: Ag) flat detector is 17 cm × 17 cm. The pixel size of the CCD camera is 41 μm × 41 μm. The purpose of the shielding material is to prevent the motor from directly exposing under high intensity neutrons. The rotating and moving stage is controlled by a computer, which can move or rotate the phantom at a certain distance or angle. We have implemented 35 times rotation for each phantom to take radiography images, in which the rotation step is 10°. The exposure time in each direction is 60 s.

Table 8 shows the reconstructed results of experimental data. Radiography images taken in the initial angle are also listed in the table. In the reconstruction, to check the performance of the IAGA-SC algorithm in few view reconstruction, the radiography images taken in five view angles (initial angle, initial angle + 60°, initial + 90°, initial + 120°, initial + 150°) are used to produce the projection data, in which the slice thickness is 4 mm. The results reconstructed by the ASD-POCS algorithm are also shown as a comparison. Relatively optimal parameters are also selected for the ASD-POCS algorithm, which are listed in table 5 of section 3.2.

Table 8. Reconstructed results of experimental data.

Reference	Radiography	ASD-POCS	Binarization	IAGA-SC	Binarization
		$c = 0.9651, d = 0.277$	$c = 0.9541, d = 0.3095$	$c = 0.9788, d = 0.205$	$c = 0.9718, d = 0.237$
		$c = 0.8429, d = 0.541$	$c = 0.8108, d = 0.6087$	$c = 0.8724, d = 0.5$	$c = 0.8707, d = 0.5135$

The parameters for the IAGA-SC algorithm are the same as are shown in table 2 of section 2.5.3.

The results show that the IAGA-SC algorithm has better performance than the ASD-POCS algorithm in experimental data reconstruction. For core flow, the shape of the object reconstructed by the ASD-POCS algorithm is a bit distorted, because the distribution of the projection direction used for reconstruction is not uniform. In this case, the shape of the object reconstructed by the IAGA-SC algorithm is much better, which just proves the powerful ability of the IAGA-SC algorithm in restoring the shape of the object. For three 'bubbles' flow, to achieve the lowest d in reconstruction with the ASD-POCS algorithm, the information of the smallest 'bubble' suffers certain loss especially for results through the binarization process, where the smallest 'bubble' almost disappears. Meanwhile the IAGA-SC algorithm with binarization can restore such a 'bubble' clearly due to the generally binary feature of results reconstructed by the IAGA-SC algorithm.

5. Discussion and conclusion

The IAGA-SC algorithm proposed in this paper is a powerful tool to implement CT reconstruction for two-phase flow. Its advantages can be summarized as four aspects: firstly, the image obtained by single time reconstruction is of binary value, which is in accordance with the natural feature of the two-phase flow, although the five times average may introduce some non-binary information to border regions; secondly, for simply connected flow regimes, especially for stratified flow, its reconstruction accuracy is much higher than that of the ASD-POCS algorithm; thirdly, for complex 'bubble' flow, it shows a greater advantage than the ASD-POCS algorithm, moreover, the advantage is inclined to be more obvious as the number of 'bubbles' increases; lastly, its ability to restore the shape of the object is much better than the ASD-POCS algorithm. In addition, the proposed algorithm has a good property in resisting statistical noise. The fundamental reason for its excellent performance lies in the fact that the algorithm has made full use of the prior information of the two-phase flow

as well as employing an advanced evolution strategy so that it can evolve towards a convergence direction.

It is effective to convert the multi-objective optimization problem to the single one by linear weighted summation. However, since the weight coefficient α determines the balance between the fidelity term and sparsity constraint term, an inappropriate α may result in unideal results. While the selection of α is empirical, this is one disadvantage of the IAGA-SC algorithm. Another disadvantage of the IAGA-SC algorithm is that it is relatively highly time consuming; for three 'bubbles' flow in an experiment as an example, a single time reconstruction takes 11 533 s with the IAGA-SC algorithm, compared to 308 s with the ASD-POCS algorithm under the computation condition: CPU: i7-4790, 3.6 GHz; RAM: 8 G (single-threaded model). In consideration of the acquisition time (60 s per projection) and five times average, the total time to obtain one image is 57 965 s with the IAGA-SC algorithm in the current experiment. Although it is a long way from real time imaging, the acquisition time can be reduced by employing a neutron source with much higher intensity, and the problem of reconstruction time will hopefully be solved by the development of parallel computation technology, such as GPU, etc. Our following research interest will be focused on promoting the computation efficiency of the proposed IAGA-SC algorithm.

As a powerful reconstruction algorithm, the IAGA-SC algorithm can also be applied to other types of two-phase flow CT, like electrical capacitance tomography (ECT) and electrical impedance tomography (EIT), etc. It is worth mentioning that the pixel size of the reconstructed images described in this paper is about 355 μm $\times$ 355 μm, and it can satisfy the accuracy of actual two-phase flow CT. Therefore, the proposed reconstruction algorithm has a potentially practical value.

Acknowledgments

Appendix

Pseudo codes of the IAGA-SC algorithm:

Begin

Initial parameters: P, G, T, S, α, b, p_0, P_{c1}, P_{c2}, P_{c3}, P_{m1}, P_{m2}, P_{m3}

Initial population by 0 or 1 randomly

gen = 1, i = 0, j = 0, m = 1, n = 1, Pr = 2255, N = 199

While gen < G **and** gen < S **Do**

    While i < P-2 **Do**

        // selection

        While j < 2 **Do**

            Selecting T individuals randomly

            Comparing fitness value *f* of selected individuals

            If random (0, 1) < p_0 **Do**

              The individual with maximum *f* is selected

            Else Do

              Selecting an individual from the population randomly

            End

            j = j + 1

        End

        // crossover

        Calculating crossover probability P_c

        If random (0, 1) < P_c **Do**

          num1 = randomN

          If random01 ==0 **Do**

            Exchanging the num1 row of selected two individuals

          Else Do

            Exchanging the num1 column of selected two individuals

          End

        End

        If random (0, 1) < P_c **Do**

          num1 = randomN

          num2 = randomN

          If random01 ==0 **Do**

            Exchanging the num1 row of the first selected individual with num2 row of the second selected individual

          Else Do

            Exchanging the num1 column of the first selected individual and num2 column of the second selected individual

          End

        End

        // mutation

        Calculating mutation probability P_m

        k = i

        While k < i + 2 **Do**

            Selecting the *kth individual*

            While m < N + 1 **Do**

               While n < N + 1 **Do**

                 Calculating the average value *A* of neighborhood pixels for pixel (m, n)

                 If random (0, 1) < P_m **Do**

                   If random (0, 1) > *A* **Do**

                     The value of current pixel (m, n) =0

                   Else Do

                     The value of current pixel (m, n) =1

                   End

                 End

                 n = n + 1

              End

              m = m + 1

            End

```
            k = k + 1
        End
        Preserving the best individual
        Individual of next generation = individual of current generation
        i = i + 2
    End
    gen = gen + 1
End
```

ORCID iDs

Huasi Hu https://orcid.org/0000-0002-4983-3703

References

[1] Hu B, Stewart C, Hale C P, Lawrence C J, Hall A R W, Zwiens H and Hewitt G F 2005 *Exp. Fluids* **39** 667–78

[2] Hampel U, Bieberle A, Hoppe D, Kronenberg J, Schleicher E, Suhnel T, Zimmermann F and Zippe C 2007 *Rev. Sci. Instrum.* **78** 103704

[3] Heindel T J, Gray J N and Jensen T C 2008 *Flow Meas. Instrum.* **19** 67–78

[4] Sakata I, Ueda T, Murakawa H, Sugimoto K, Asano H, Takenaka N, Yasuda R, Tomura T and Shiozawa M 2009 *Nucl. Instrum. Methods* A **605** 131–3

[5] Zboray R, Adams R, Cortesi M and Prasser H M 2014 *Nucl. Eng. Des.* **273** 10–23

[6] Sidky E Y, Kao C M and Pan X H 2006 *J. X-Ray Sci. Technol.* **14** 119–39

[7] Kisner S J, Haneda E, Bouman C A, Skatter S, Kourinny M and Bedford S 2012 *Proc. Computational Imaging X* **8296** 82960f

[8] Andersen A H and Kak A C 1984 *Ultrason. Imaging* **6** 81–94

[9] Yang W Q, Spink D M, York T A and McCann H 1999 *Meas. Sci. Technol.* **10** 1065–9

[10] Kawata S and Nalcioglu O 1985 *IEEE Trans. Med. Imaging* **4** 65–71

[11] Miller M I, Snyder D L and Miller T R 1985 *IEEE Trans. Nucl. Sci.* **32** 769–78

[12] Byrne C L 1993 *IEEE Trans. Image Process.* **2** 96–103

[13] Candes E J and Tao T 2006 *IEEE Trans. Inf. Theory* **52** 5406–25

[14] Donoho D L 2006 *IEEE Trans. Inf. Theory* **52** 1289–306

[15] Sidky E Y and Pan X C 2008 *Phys. Med. Biol.* **53** 4777–807

[16] Yang W Q and Peng L H 2003 *Meas. Sci. Technol.* **14** R1–3

[17] Xue Q A and Wang H X 2010 *IEEE I2MTC. Proc.* 1510–14

[18] Whitley D 1994 *Stat. Comput.* **4** 65–85

[19] Mera N S, Elliott L and Ingham D B 2003 *Inverse Probl. Eng.* **11** 105–21

[20] Srinivas M and Patnaik L M 1994 *IEEE Trans. Syst. Man Cybern.* **24** 656–67

[21] Hjertaker B T and Johansen G A 2008 *AIP Conf. Proc.* **1050** 163–74

[22] Lo S C B 1988 *IEEE Trans. Med. Imaging* **7** 355–63

[23] Mueller K, Yagel R and Wheller J J 1999 *IEEE Trans. Med. Imaging* **18** 519–37

[24] Siddon R L 1985 *Med. Phys.* **12** 252–5

[25] Quarteroni R, Sacco A and Saleri F 2000 *Numerical Mathematics* (New York: Springer) pp 349–50

[26] Li Y Y and Santosa F 1996 *IEEE Trans. Image Process.* **5** 987–95

[27] Yu W and Zeng L 2014 *PLoS One* **9** e109345

[28] Chen Z Q, Jin X, Li L and Wang G 2013 *Phys. Med. Biol.* **58** 2119–41

[29] Zhou M and Sun S D 1990 *Genetic Algorithms: Theory and Applications* (Beijing: National Defence Industry Press) pp 46–55

[30] Chen Y W, Nakao Z and Arakaki K 1997 *Opt. Rev.* **4** 209–15

[31] Eskicioglu A M and Fisher P S 1995 *IEEE Trans. Commun.* **43** 2959–65

[32] Otsu N 1979 *IEEE Trans. Syst. Man Cybern.* **9** 62–6

[33] Lohvithee M, Biguri A and Soleimani M 2017 *Phys. Med. Biol.* **62** 9295–321